Electrothermal dynamics-conscious many-objective modular design for power-split plug-in hybrid electric vehicles

Li, Ji; Liu, Kailong; Zhou, Quan; Meng, Jinhao; Ge, Yunshan; Xu, Hongming

DOI:
10.1109/TMECH.2022.3156535

Electrothermal Dynamics-conscious Many-objective Modular Design for Power-split Plug-in Hybrid Electric Vehicles

Ji Li, *Member, IEEE,* Kailong Liu, *Member, IEEE,* Quan Zhou, *Member, IEEE,* Jinhao Meng, *Member, IEEE,* Yunshan Ge, and Hongming Xu

***Abstract*--This paper proposes an improved modular design methodology of a power-split plug-in hybrid electric vehicle (PHEV) that introduces an advanced electrothermal coupled model and a temperature-related sub-objective to simultaneously reveal battery thermal and electrical dynamics in the modular design. Considering to provide customers with more optimal configuration solutions, a Pareto-augmented collaborative optimization (PACO) scheme is designed that integrates three benchmarking many-objective evolutionary algorithms (MOEAs) to expand the distribution of an approximated Pareto frontier composed of the best solution set. Two realistic worldwide harmonized light vehicles test cycles are separately reproduced by two trained drivers on a chassis dynamometer to test the robustness of the optimized vehicle system. The simulation results demonstrate that the MOEA based on decomposition (MOEA/D) in the PACO is the main contributor for PHEV modular design because it lessens the generational distance by at least 2.7% and enlarges the hypervolume by at least 17.6%, compared to the elitist non-dominated sorting genetic algorithm and improved strength Pareto evolutionary algorithm. In the modular adaptation for different user types, the PHEV system optimized by the PACO can regulate cell temperatures ($27.5-38.3$℃) of all user types within a safe and efficient working zone ($0-55$℃).**

***Index Terms*--electrothermal battery model; many-objective evolutionary algorithm; modular design and adaptation; power-split plug-in hybrid electric vehicle.**

NOMENCLATURE

M	Gross mass
A_f	Windward area
R_{wh}	Tire rolling radius
C_d	Air drag coefficient
i_0	Reducer ratio
η_{i0}	Differential efficiency
τ_d	Torque demand
n_d	Rotation speed demand
g	Gravitational constant
δ	Coefficient of rolling friction
θ	Slope grade
u	Vehicle speed
$P_{f,L_{ice}}$	Equivalent power of the fuel consumption
L_{ice}	Displacement of the candidate engine
L^*	Displacement of the baseline engine
$\dot{m}_f$	Instantaneous fuel consumption
H_f	Heat value for gasoline oil
SoC	State of charge
I	Battery current
T_s	Battery surface temperature
T_c	Battery internal temperature
C_n	Battery nominal capacity
T_{amb}	Ambient temperature
V_{oc}	Open circuit voltage
$\boldsymbol{\xi}$	Power-split vector
τ_{mot}	Trans-motor torque
n_{mot}	Trans-motor speed
τ_{ice}	ICE torque
n_{ice}	ICE speed
P_{gen}	ISG power
χ_i	Proportionality factor
SoC^*	Scaling coefficient of the battery module's SoC
$\phi_{i,\alpha}$	Control parameters for ICE
$\phi_{i,\beta}$	Control parameters for ISG
Num_{bc}	Number of battery cells
C_{cell}	Cost of one battery cell
T_{avg}	Average temperature of battery cells
$\boldsymbol{\theta}^*_{size}$	Vector of modular component sizing parameters
$\boldsymbol{\theta}^*_{ems}$	Vector of power-split control parameters

I. INTRODUCTION

GROWING concerns for transport-related air pollution and global warming have thrust the automotive industry to seek low-cost carbon emission reduction solutions [1], [2]. In this context, plug-in hybrid electric vehicles (PHEVs) are increasingly seen as an efficient means of transportation in mitigating the growing air quality concerns of exhaust gas emissions from traditional internal combustion engines (ICE) [3]. Compared to a pure electric vehicle, a PHEV normally has more mileage, and more flexibility in the control of emission actuation, e.g., a green zone/district in a city, or to the polluting mode when the resulting emissions have less effect [4].

Modular design allows vehicular products to be customized, upgraded, repaired and for parts to be reused in a fast and low-cost way. In 2012, the Volkswagen Group released the well-known MQB platform [5] that enables to sharing a common engine-mounting core for various drivetrains, as well as reducing weight. In Ref. [6], a model-based sizing tool for a hybrid wind-diesel-photovoltaic-battery system by empirical approach is developed to analyze the performance and life-cycle cost. Besides, sizes of the engine and generator can be also determined according to the average electrical power

This work was supported by the High Value Manufacturing Catapult project under grant No. 160080 CORE, the Fundamental Research Funds under grant YJ202013 and the China Postdoctoral Science Foundation under Grant 2020M673218. *(Corresponding authors: Kailong Liu)*

Ji Li, Quan Zhou, and Hongming Xu are with the Department of Mechanical Engineering, the University of Birmingham, Birmingham, U.K. (e-mail: Ji.Li@ieee.org; q.zhou@bham.ac.uk; h.m.xu@bham.ac.uk). Kailong Liu is with Warwick Manufacturing Group, the University of Warwick, Coventry, U.K. (e-mail: kliu02@qub.ac.uk; kailong.liu@warwick.ac.uk). Jinhao Meng is with the College of Electrical Engineering, Sichuan University, Chengdu, China (e-mail: scmjh2008@163.com). Yunshan Ge is with School of Mechanical Engineering, the Beijing Institute of Technology, Beijing, China. (geyunshan@bit.edu.cn)

requirement in various driving cycles [7].These conventional modular design methods depend on the experts' experience [8], while the design results are determined by the design of experiments [9]. Since multiple disciplines may be involved in such a complicated hybrid powertrain, e.g., electrical, chemical, mechanical, etc. it is extremely difficult to size its components manually or analytically because they rely on the sizing experience or simple calculation [10].

Rapid development in informatics enables a faster and more efficient fashion for intelligent modular design of vehicles. As the core of intelligent modular design, a computationally efficient algorithm is the guarantee for acquiring the desirable powertrain specifications and control parameters [11]. Convex optimization has been widely developed for HEV component sizing [12], [13], because it can overcome the limitation of size in the optimization problem. Nevertheless, developers must have strong skills in convex modelling to reformulate the optimization issue into a convex form. Heuristic algorithms are often used to solve such an NP-complete problem. Li et al. and Zhou et al. study an enhanced particle swarm optimization algorithm with chaotic attraction strategy for energy management system design of on-road [14], [15] and off-road vehicles [16]. Such single-objective optimization algorithms are difficult to establish a well-distributed Pareto frontier, especially when the objectives are more than two. Another idea is to formulate vehicle optimal design as an optimal control problem e.g., co-optimization of energy management and driving speed [17], but its optimality is difficult to guarantee.

Battery is primary energy storage source supplied for PHEVs, which would present various electrical and thermal dynamics during its operations [18]. In this context, numerous modelling techniques have been developed [19] to capture the electrical or thermal behaviors of batteries, which can be primarily divided into the electrical model, thermal model, and coupled model. For the electrical model, due to the superiority in terms of computational efficiency, equivalent circuit models (ECMs), i.e., resistor-capacitor (RC) ECMs [20] and fractional-order ECMs [21], have been widely used to capture the electrical behavior in battery real-time applications. For the thermal model, through assuming the heat generation is evenly distributed within batteries, two-stage thermal modelling has become an effective path to describe the thermal dynamics of both battery surface and interior [22]. Several coupled electrothermal models have been also designed to describe the strongly coupled relation between battery electrical and thermal behaviors [23]. Among various types of coupled models, the lumped-parameter electrothermal models [24] with reduced order and a relatively small number of model parameters are popular in practice such as battery energy and charging management [25], [26]. Even so, the thermal dynamics of batteries is often ignored in the system-level modular design of PHEVs owing to a heavy increase in system complexity.

To simultaneously reveal battery thermal and electrical dynamics in the PHEV modular design, this paper proposes an improved modular design methodology that introduces an advanced electrothermal coupled model and a temperature-related sub-objective. The model contains a second-order RC sub-model and an extra two-state thermal sub-model that can well capture both battery electrical and thermal dynamics. Considering to provide customers with more optimal configuration solutions, a Pareto-augmented collaborative optimization scheme is designed that integrates three benchmarking many-objective evolutionary algorithms (MOEAs). Conversely, this scheme absorbs their advantages in solving such a many-objective problem to construct and expand an approximated Pareto frontier which is closer to the ground truth for providing more design options for customers. Finally, the optimal combination of module specifications and control parameters can be determined by the desirability function.

The rest of this paper is organized as follows: the powertrain and scalable modules to be studied in this paper are analyzed in section II. The optimization problem is formulated in Section III. The improved modular design methodology with electrothermal dynamics-conscious is described in section IV. Section V explains the experimental process of the studied driving cycle and discusses the results of 1) many-objective optimization; 2) vehicle system robustness; and 3) the modular adaptation. Conclusions are summarized in section VI.

II. Powertrain and Scalable Modules

The power-split plug-in hybrid powertrain for this research comprises an internal combustion engine (ICE), an integrated starter-generator (ISG), a trans-motor (i.e., electric motor with float stator [27]) which is used for speed coupling. As illustrated in Fig. 1, this powertrain topology enables to decoupling speeds of the two powerplants. Therefore, the speed of both the powerplants can be chosen freely. The vehicle data in Table I was sourced from ADVISOR software for powertrain system analysis and design.

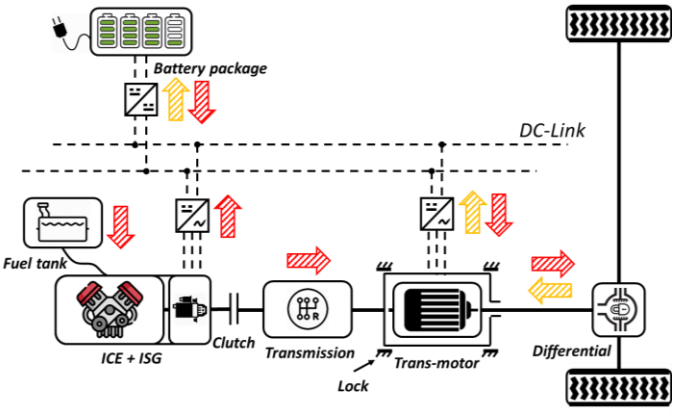

Fig. 1. The architecture of power-split plug-in hybrid powertrain

TABLE I
MAIN PARAMETERS OF THE VEHICLE MODEL

Symbol	Parameters	Values
M	Gross mass	1,500 kg
A_f	Windward area	2 m^2
R_{wh}	Tire rolling radius	0.3 m
C_d	Air drag coefficient	0.3
i_0	Reducer ratio	3.75
η_{i0}	Differential efficiency	0.95

By controlling the disengagement/engagement of the clutch and lock, the PHEV can work on three operational modes, i.e., EV mode, parallel mode, and series mode. If the clutch is

disengaged, and the lock is engaged, the PHEV will work at the EV mode like an electric vehicle. If the clutch is engaged, and the lock is disengaged, the PHEV will work at the parallel mode where the engine is used for joint propulsion. If the clutch is disengaged, and the lock is engaged, the PHEV will work at the series mode where the engine is used for charging the battery in case the lower SoC causes the motor not to work especially when the ICE cannot meet the high-speed demand.

A backwards-facing vehicle model considering longitudinal dynamics is used in this study. The torque demand τ_d and rotation speed demand n_d after a bi-level-gear speed reducer are:

$$\left.\begin{aligned}\tau_d &= \left(\delta ma + \frac{C_d A_f u^2}{21.15} + mgsin\theta + mgfcos\theta\right)\cdot\frac{R_{wh}}{i_0\cdot\eta_{i0}}\\ n_d &= 9.55\cdot\frac{u}{3.6\cdot R_{wh}}\end{aligned}\right\} \quad (1)$$

where, $g = 9.81 m/s^2$ is gravitational constant; $\delta = 1$ is the equivalent mass inertia; $f = 0.015$ is the coefficient of rolling friction; u is the vehicle speed in km/h which is defined by driving cycles; 21.15 is a conversion coefficient under windless condition; $\theta = 0$ is slope grade; 9.55 is a conversion coefficient from radian per second to revolution per minute; 3.6 is a conversion coefficient from meter per second to kilometer per hour. For this model to be valid, we assume the PHEV has an available energy budget for a particular journey.

A. Internal Combustion Engine Module

An empirical ICE model from a Saturn 1.9 L spark-ignition engine validated by Argonne National Laboratory [28] is selected as the baseline for the modular design. According to Willans approximation method [29], the maximum power of the engine can be scaled by considering its displacement, and thus, the equivalent power of the fuel consumption is scaled by the displacement of the engine, L_{ice}

$$P_{f,L_{ice}} = \frac{L_{ice}}{L^*}\cdot H_f\cdot\dot{m}_f(T_{ice}, n_{ice}) \quad (2)$$

where L_{ice} is the displacement of the candidate engine in liters; L^* is the displacement of the baseline engine in liters; $\dot{m}_f$ refers to the instantaneous fuel consumption, g/s; and H_f refers to the heat value for gasoline oil, which is 46×10^6 J/kg.

B. Electrothermal Coupled Lithium-ion Battery Module

To well capture both battery electrical and thermal dynamics in this study, an advanced electrothermal coupled model is established, as illustrated in Fig. 2. The model contains a second-order RC sub-model and a two-state thermal sub-model. For this electrothermal model, the battery's state of charge (SoC), $SoC(t)$ and voltages $(V_1(t), V_2(t))$ of two RC parts versus time t are described by (3a) to (3c) respectively, while the surface temperature $T_s(t)$ and internal core temperature $T_c(t)$ versus t are captured by (3d) and (3e) respectively.

$$\frac{dSoC(t)}{dt} = \frac{I(t)}{C_n} \quad (3a)$$

$$\frac{dV_1(t)}{dt} = \frac{V_1(t)}{R_1(t)C_1(t)} + \frac{I(t)}{C_1(t)} \quad (3b)$$

$$\frac{dV_2(t)}{dt} = \frac{V_2(t)}{R_2(t)C_2(t)} + \frac{I(t)}{C_2(t)} \quad (3c)$$

$$\frac{dT_s(t)}{dt} = \frac{T_{amb} - T_s(t)}{R_u C_s} - \frac{T_s(t) - T_c(t)}{R_c C_s} \quad (3d)$$

$$\frac{dT_c(t)}{dt} = \frac{T_s(t) - T_c(t)}{R_c C_c} + \frac{Q(t)}{C_c} \quad (3e)$$

where $I(t)$, $R_1(t)C_1(t)$, $R_2(t)C_2(t)$ are the current, parameters of R_1C_1 pair and R_2C_2 pair versus t, respectively. C_n represents the battery normal capacity, T_{amb} means the ambient temperature, R_u, R_c, C_s, C_c are the model's thermal parameters. Here the heat generation $Q(t)$ in (3e) is calculated by:

$$Q(t) = I(t)T_c(t)\frac{dOCV(t)}{dT_c(t)} + I(t)\big(V(t) - OCV(t)\big) \quad (4)$$

The open circuit voltage (OCV) presents a nonlinear relation with the battery SOC level. According to this electrothermal model, battery terminal voltage $V(t)$ can be obtained by:

$$V(t) = OCV\big(SoC(t)\big) + R(t)I(t) + V_1(t) + V_2(t) \quad (5)$$

The exact parameter values of this battery electrothermal coupled model are referred to [30] for the A123 26650 battery. In this study, coolant is adopted, which can be expressed in the electrothermal model by a convection resistance, R_u, as considered in [31]. The established model has been well validated, with a satisfactory accuracy of less than 20 mV rooted mean square error (RMSE) of terminal voltage, while both internal and surface temperatures present less than 1°C RMSEs. In the battery module, all these cells are connected in series with the unified current as the similar strategies deployed in many PHEV applications such as [32].

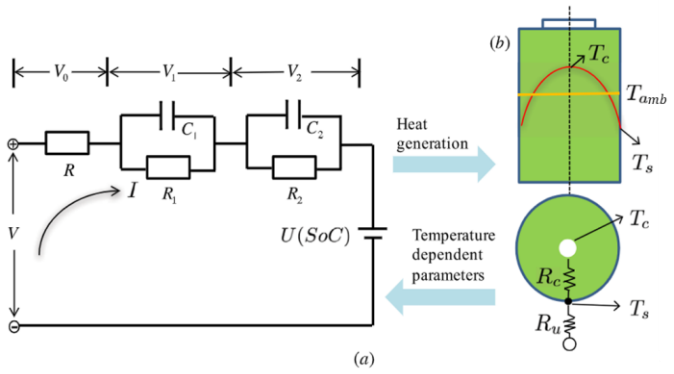

Fig. 2. Electrothermal model of a cylindrical Li-ion battery [33]: a) Equivalent circuit electrical model; and b) Lumped thermal model

C. Energy Management Module

The energy management module adopts a typical state machine [34] to control the transition between three operation modes as shown in Fig. 3. This method is robust and easy to implement that is commonly used in automotive industry.

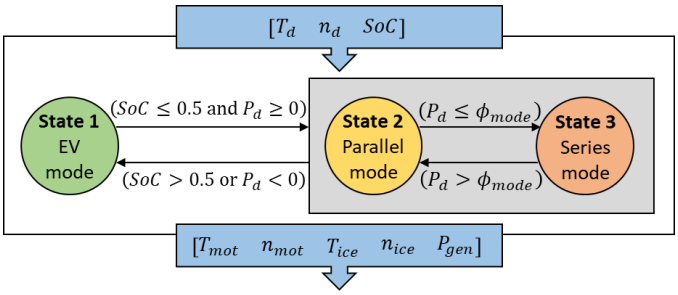

Fig. 3. Overview of states of mode transition state machine

The state machine controller has three inputs: vehicle torque demand, T_d, speed demand, n_d, and battery state of charge, SoC. The output of the state machine is a power-split vector:

$$\boldsymbol{\xi} = [T_{mot} \quad n_{mot} \quad T_{ice} \quad n_{ice} \quad P_{gen}] \tag{6}$$

where T_{mot} and n_{mot} are the torque demand and speed demand of the trans-motor, respectively; and P_{gen} is the power demand of the ISG.

In the EV mode (when $SoC > 0.5$ or $P_d < 0$), the PHEV will work like a battery electric vehicle, therefore, the power-split vector under the EV mode is:

$$\boldsymbol{\xi} = [\tau_d \quad n_d \quad 0 \quad 0 \quad 0] \tag{7}$$

In the series and parallel modes (when $SoC \leq 0.5$ and $P_d \geq 0$), switching between series and parallel modes are governed by the power demand, P_d, and a control parameter, ϕ_{mode}. If $P_d > \phi_{mode}$, the vehicle will work on parallel mode otherwise the vehicle will work on series mode. The power-split vector for series mode is:

$$\boldsymbol{\xi} = \left[\tau_d \quad n_d \quad \tau_{ice}^{'}(P_{gen}) \quad n_{ice}^{'}(P_{gen}) \quad P_{gen^+} \cdot \chi_2\right] \tag{8}$$

The power-split vector for parallel mode is:

$$\boldsymbol{\xi} = [\tau_d \quad n_d \cdot (1-\chi_1) \quad T_d \quad n_d \cdot \chi_1 \quad 0] \tag{9}$$

where, $\tau_{ice}^{'}$ and $n_{ice}^{'}$ are optimal torque and speed of the ICE, in which they are retrieved based on the location of demand power of the ISG P_{gen} in the optimal efficiency curve of the ICE; P_{gen}^{+} is the maximum power of the ISG; χ_i (i =1 or 2) is a proportionality factor determined by SoC as follows, χ_1 and χ_2 are for ICE control and ISG control, respectively [3].

$$\chi_i(SoC) = \begin{cases} 1, & SoC \in [0,0.2] \\ \left\{1 + \exp\left[\left(\frac{SoC}{SoC^*} + \phi_{i,\beta}\right)\phi_{i,\alpha}\right]\right\}^{-1}, & SoC \in (0.2,0.5] \\ 0, & SoC \in (0.5,1] \end{cases} \tag{10}$$

where, SoC^* is a scaling coefficient of the battery module's SoC to ensure search efficiency of parameters $\phi_{i,\beta}$ and $\phi_{i,\alpha}$ in the PHEV modular design; and $\phi_{i,\alpha}$ (i=1 or 2) $\in [0.01,50]$ and $\phi_{i,\beta}$ (i=1 or 2) $\in [-6,6]$ are four control parameters introduced here to enable optimization of cut-in timing and conversion speed of the ICE and ISG. They separately define the position and slope of the curve in this logistic function.

III. Problem Formulation

This research focuses on three optimization objectives: 1) the final energy consumption from the fuel tank and the battery module; 2) total cost of the ICE and battery module; and 3) integral squared error (ISE) of average temperature of battery cells and the ambient temperature. The definition of each objective is given in order as follows. Considering energy-saving efficiency, the first objective is formulated as:

$$J_1 = \int_0^t \left(P_{f,L_{ice}} + \mathrm{Num}_{bc} \cdot V_{oc}(SoC) \cdot I_{bc}\right) dt \tag{11}$$

where, $P_{f,L_{ice}}$ is the equivalent power of the fuel consumption; Num_{bc} is the number of battery cells; V_{oc} is open circuit voltage and I_{bc} is the current. The cost of components is the second objective that directly affects the final pricing of the vehicle and further customers' acceptance. It can be described as:

$$J_2 = 12P_{ice}^{max}(L_{ice}) + 424 + C_{cell} \cdot \mathrm{Num}_{bc} \tag{12}$$

where, the cost estimation method for a regular engine is adopted from EPRI and Golbuff's study [35], [36], wherein C_{ice} is the cost (USD) of the engine whose maximum power is P_{ice}^{max}; 424 (USD) is a baseline coefficient for regular engine cost; C_{cell} is the cost of one battery cell and its number Num_{bc}.

In real battery applications, the temperature difference with the ambient temperature is an important indicator to reflect battery temperature rise, which could further benefit the evaluation of the battery thermal characteristics, as considered in [26]. To ensure safe and efficient use of the battery module, the third objective is formulated as ISE of the average temperature of battery cells and the ambient temperature. Since ISE can penalize large errors more than smaller ones, control systems specified to minimize ISE of average temperature of battery cells and the ambient temperature will tend to eliminate large overshooting over a safe threshold quickly but will tolerate small oscillation persisting for a long period of time.

$$J_3 = \int_0^{t_{end}} \left(T_{avg}(t) - T_{amb}\right)^2 dt \tag{13}$$

where, T_{amb} is the ambient temperature and T_{avg} is the average temperature of battery cells. Consequently, the many-objective design problem of the studied PHEV is described by:

$$[\boldsymbol{\theta}_{size}^* \quad \boldsymbol{\theta}_{ems}^*] = \arg\min(J_1 \quad J_2 \quad J_3) \tag{14}$$

in which

$$\left.\begin{aligned} \boldsymbol{\theta}_{size}^* &= [L_{ice}^* \quad \mathrm{Num}_{bc}^*] \\ \boldsymbol{\theta}_{ems}^* &= \left[\phi_{1,\alpha}^* \quad \phi_{1,\beta}^* \quad \phi_{2,\alpha}^* \quad \phi_{2,\beta}^* \quad \phi_{mode}^*\right] \end{aligned}\right\} \tag{15}$$

where, $\boldsymbol{\theta}_{size}^*$ indicates a vector of component sizing parameters; and $\boldsymbol{\theta}_{ems}^*$ indicate a vector of power-split control parameters. To ensure the convergence speed of each objective at the same scale, all input variables need to be normalized first. During the optimization process, the system must obey the following constraints.

$$s.t. \begin{cases} SoC \in [0.2,0.8] \\ n_{mot} \in [0, n_{mot^+}] \\ \tau_{mot} \in [\tau_{mot^-}, \tau_{mot^+}] \\ P_{ice} \in [0, P_{ice^+}] \\ P_{gen} \in \left[0, P_{gen^+}\right] \end{cases} \tag{16}$$

where the SoC must be regulated in [0.2,0.8] for safe and efficient use; n_{mot^+} is the maximum speed of the traction motor; T_{mot^-} and T_{mot^+} are minimum and maximum torque of the traction motor, respectively. P_{ice^+} is the maximum power of the ICE; and P_{gen^+} is the maximum power of the ISG. All power machines should operate in their working ranges.

IV. Electrothermal Dynamics-conscious Many-objective Modular Design

The working principle of the many-objective modular design methodology with electrothermal dynamics-conscious in this study is illustrated in Fig. 4.

The block of inputs, as presented in Fig. 4(a), provides information from the real-world measurements, standards, and requirements, for the formulation of the many-objective optimization problem. The driving cycle used for optimization is two consecutive repetitions of the worldwide harmonized light vehicle test cycle (2×WLTC). The block of the optimization, given in Fig. 4(b), is the flow chart of the Pareto-augmented collaborative optimization (PACO) scheme that integrates three benchmarking many-objective evolutionary algorithms (MOEAs) to co-solve the formulated many-

objective optimization problem. The block of Pareto analysis and result verification presented in Fig. 4(c), utilizes the desirability function to derive the best compromise solution from the approximated Pareto frontier resulting from the PACO. Finally, the optimized system adaptability will be evaluated by using the laboratory-made WLTCs, in which the collection process is elaborated in the next section.

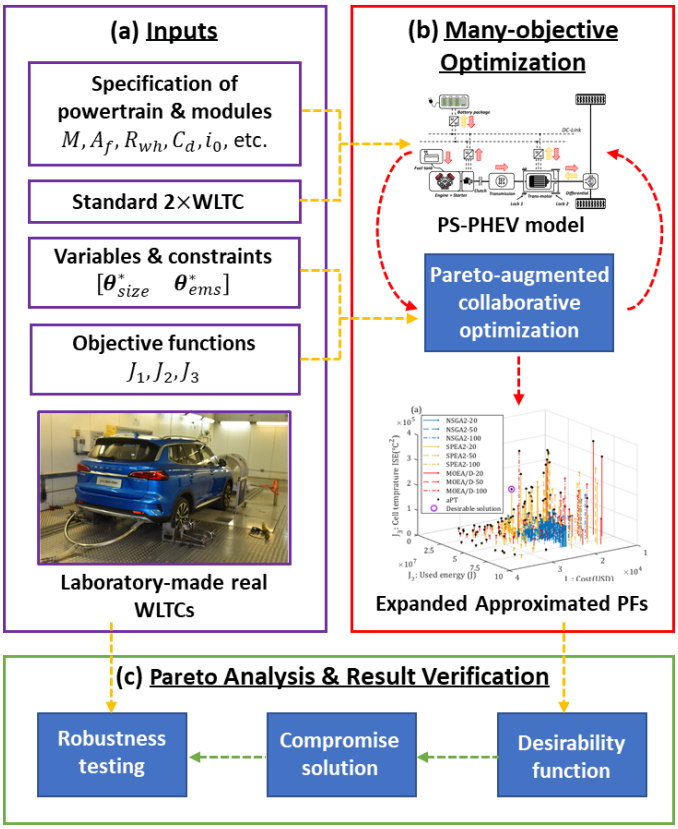

Fig. 4. Working principle of the improved modular design methodology with electrothermal dynamics conscious

A. Pareto-Augmented Collaborative Optimization

It is well acknowledged that combining or integrating optimization algorithms, especially ones with large differences in computing mechanism could greatly improve the Pareto frontier [37], [38]. In light of this, the PACO scheme is designed with integrating three benchmarking many-objective evolutionary algorithms (MOEAs) to expand the distribution of an approximated Pareto frontier composed of the best solution set. They are the elitist non-dominated sorting genetic algorithm (NSGA2) which introduces a selection operator that creates a mating pool by combining the parent and offspring populations and selecting the best solutions, improved strength Pareto evolutionary algorithm (SPEA2) which incorporates a fine-grained fitness assignment strategy, a density estimation technique, and an enhanced archive truncation method, and MOEA based on decomposition (MOEA/D) which explicitly decomposes the many-objective optimization problem into scalar optimization subproblems and solves these subproblems simultaneously by evolving a population of solutions. With help of the PACO scheme, the approximated PF is determined by sorting three individual estimated PFs calculated by NSGA2, SPEA2, and MOEA/D, respectively.

B. Desirability Function Approach

To determine module specifications and control parameters, the desirability function is employed to obtain the best compromise solution from the Pareto frontier based on decision makers, as shown in Fig. 4(c). The method adopted by Pasandideh et al. [43] computes a penalty score α for each objective vector in a set of the approximated PF. Consequently, the solution with the minimum α is the best compromise. The expressions of the desirability function are presented as follows.

$$\min_{K\in PF} \alpha\big(J(K)\big) = \min_{K\in PF} \sum_{i=1}^{3} w_i \frac{J_i(K) - J_i^{\min}}{J_i^{\max} - J_i^{\min}} \tag{17}$$

$$\begin{cases} J = [J_1 \quad J_2 \quad J_3] \\ K = [\boldsymbol{\theta}^*_{size} \quad \boldsymbol{\theta}^*_{ems}] \\ \sum_{i=1}^{3} w_i = 1 \text{ and } w_i \geq 0 \end{cases} \tag{18}$$

where $J_i^{\max}$ and $J_i^{\min}$ denote the maximum and minimum values of the objective function J_i on the approximated PF; K is the variable vector; w_i stands for a weight factor given by the decision-maker.

V. Results and Discussion

For evaluation purposes, this research adopts two realistic WLTCs separately reproduced by two trained drivers on a chassis dynamometer, as illustrated in Fig. 5(a), which is located at China Automotive Technology & Research Center.

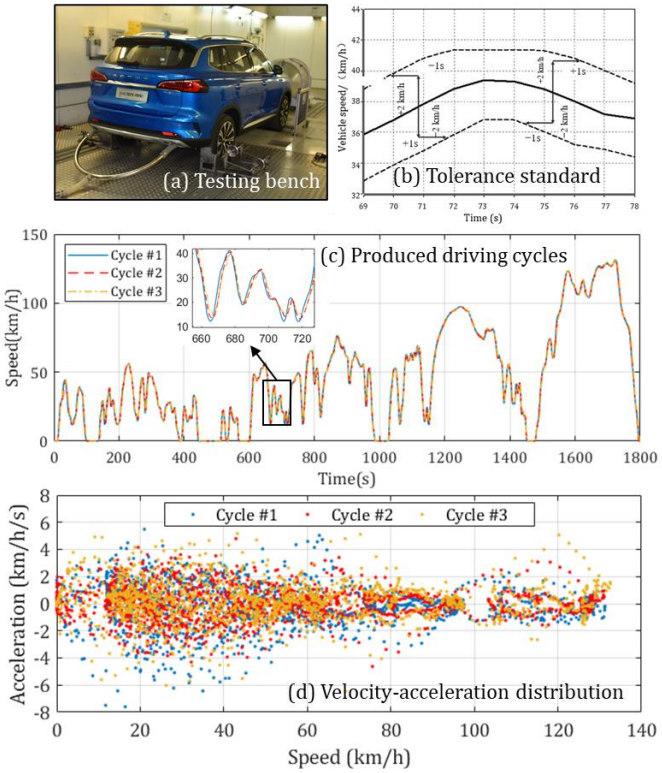

Fig. 5. Realistic WLTC reproduction process: a) chassis dynamometer testing bench; b) tolerance standard for driving tests; c) driving cycle profiles; and d) velocity-acceleration distribution

During the test, the driver should strictly abide by the tolerance standard promulgated by 'Limits and measurement methods for emissions from light-duty vehicles' (GB 18352.6). The allowable tolerance, as illustrated in Fig. 5(b), between the actual speed of the vehicle and the speed specified in the test is:

1) upper tolerance limit, +2km/h, time is within 1s and 2) lower tolerance limit, -2km/h, time is within 1s. The allowable speed error can be greater than the specified requirements, but the over-tolerance time must not exceed 1s. In addition, such out-of-tolerance cases must not exceed 10 times. Fig. 5(d) displays velocity-acceleration distribution comparison of one original (cycle #1) and two reproduced cycles (cycle #2, cycle #3). In the medium-speed and high-speed areas (70-130km/h), the acceleration of reproduction cycles is more aggressive, especially cycle #3.

A. Pareto Analysis for Many-objective Optimization

Fig. 6(a) presents the estimated PFs obtained with the PACO integrated with NSGA2, SPEA2, and MOEA/D, in which an approximated PF is obtained by calculating the nondominated set from all the estimated PF. A desirable solution (marked in a light blue circle) is calculated based on the desirability function approach with the weight factor $w = [0.4\ 0.4\ 0.2]$. For a fair comparison, all optimization algorithms set to the same population size, i.e., $N = 20{,}50{,}100$, same archive size, i.e., $\overline{N} = 50$, same probability of crossover and mutation rates, i.e., $p_{cro} = 0.7$ and $p_{mut} = 0.3$, and same termination criterion, i.e., no more than 100 iterations.

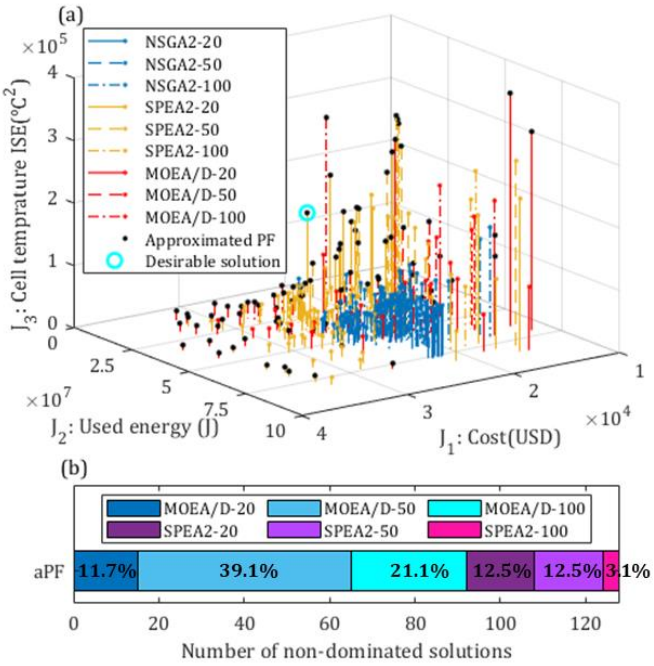

Fig. 6. Pareto frontier comparison of using three evolutionary optimization algorithms: a) estimated and approximated Pareto frontiers; and b) distribution of number of non-dominated solutions.

From the results of the scatter plot, the estimated PFs obtained by NSGA2 (marked in blue) show a smaller spread and distribution compared to those obtained by SPEA2 and MOEA/D. In conjunction with Fig. 6(b), the PACO collects more non-dominated solutions, in which there is at least 28% of the increase compared to every single algorithm. Furthermore, the MOEA/D occupies 72% non-dominated solutions in total, and SPEA2 occupies the remaining 28%, but NSGA2 does not own any non-dominated solutions in this case. In terms of population sizes, applying 50 populations in studied optimization algorithms achieves 66% dominion in the approximated PF, contrasted to those using 20 populations (23%) or 100 populations (31%).

TABLE II
OPTIMIZATION PERFORMANCE COMPARISON OVER THREE EVOLUTIONARY ALGORITHMS

Population	Optimization algorithm	GD		HV	
		Mean	SD	Mean	SD
20	NSGA2	3.42e+7	9.91e+14	2.00e-3	3.27e-6
	SPEA2	5.88e+6	2.98e+13	2.36e-1	4.87e-2
	MOEA/D	1.02e+6	9.40e+11	3.11e-1	8.56e-2
50	NSGA2	1.28e+7	1.43e+14	1.30e-2	1.46e-6
	SPEA2	1.82e+6	3.07e+12	2.62e-1	6.18e-2
	MOEA/D	1.77e+6	2.82e+12	3.08e-1	8.67e-2
100	NSGA2	4.63e+6	1.97e+13	6.10e-2	3.30e-3
	SPEA2	3.47e+6	1.14e+13	2.82e-1	1.06e-1
	MOEA/D	1.63e+6	2.51e+12	3.34e-1	7.51e-2

To quantitatively evaluate convergence and estimated PF set distribution of three studied algorithms, two commonly used optimization metrics of the generational distance (GD) [39] and hypervolume (HV) [40] are involved. Their definitions are presented in Appendix. Table II summarizes the optimization indicator performance of GD and HV over three evolutionary algorithms. Compared to NSGA2 and SPEA2, MOEA/D with better convergence and PF set distribution achieves the lowest mean value of the GD and the highest mean value of the HV for each population size. It should be noted that there are orders of magnitude gaps in the performance of NSGA2 in the mean value of the HV from the other two. This conclusion is consistent with an illustration in Fig. 6(a). Compared to NSGA2 and SPEA2, MOEA/D can lessen the generational distance by at least 2.7% and enlarge the hypervolume by at least 17.6%. Therefore, MOEA/D is a desirable solver for such a complex nonlinear optimization problem.

B. Vehicle System Performance and Robustness

Driving behavior is a primary factor that would affect fuel economy [41]. This section further examines the robustness of the vehicle system optimized by the PACO against laboratory cycles generated by different human drivers. Each case runs under the original Worldwide Harmonized Light Vehicle Test Cycle (WLTC) repeatedly for two rounds with an initial battery SoC of 0.8. The optimal results will be applied in the PHEV system for different driving scenarios i.e., Cycle #1 to #3.

Table III organizes vehicle system performance in four aspects of: 1) weighted-sum value of cost functions; 2) cost of the ICE and battery cells; 3) energy consumption; and 4) ISE of battery cell temperature. It should be noted that the weighted-sum value of cost functions is calculated based on the desirability function approach as Eq. (17). Three levels of the ambient temperature, $T_{amb} = 15°C, 25°C, 35°C$ have been investigated. From the result of cost function values, the MOEA/D wins first place eight times in nine testing scenarios (3 testing cycles * 3 levels of the ambient temperature), wherein on the basis of the NSGA2 and the SPEA2, the MOEA/D respectively reduces the cost function values by 22.23% and 9.44% on average. In the robustness testing of the PHEV system against Cycle #2 and #3, using parameters optimized by MOEA/D controls an increase of the cost function value within 31.0%. That is much lower than increases of the cost function values using parameters optimized by NSGA2 (62.9%) and SPEA2 (77.1%). In conjunction with Fig. 5(d), with an increase

TABLE III
VEHICLE SYSTEM PERFORMANCE COMPARISON

Testing cycle	Optimization algorithm	Weighted-sum value of cost functions			Cost of the ICE and battery cells (10^4 USD)			Energy consumption (10^7J)			ISE of battery cell temperature (10^4°C^2)		
		15°C	25°C	35°C	15°C	25°C	35°C	15°C	25°C	35°C	15°C	25°C	35°C
Cycle #1	NSGA2	0.614	0.687	0.602	2.021	2.403	2.329	3.234	2.499	2.930	17.27	1.668	0.496
	SPEA2	0.496	0.646	0.507	1.616	2.361	2.223	2.656	2.288	1.795	4.675	1.081	0.625
	MOEA/D	**0.434**	**0.604**	**0.506**	1.600	2.354	1.768	1.776	1.900	2.860	15.79	0.971	1.378
Cycle #2	NSGA2	0.654	0.692	0.648	2.021	2.403	2.329	3.835	2.692	3.627	11.27	0.969	0.357
	SPEA2	0.538	0.692	0.551	1.616	2.361	2.223	3.288	2.756	3.504	3.505	1.027	1.600
	MOEA/D	**0.483**	**0.688**	**0.539**	1.600	2.354	1.768	2.510	2.703	2.285	24.47	1.141	0.417
Cycle #3	NSGA2	1	0.983	0.818	2.021	2.403	2.329	6.037	3.884	5.909	69.77	9.449	2.784
	SPEA2	**0.518**	0.906	0.898	1.616	2.361	2.223	2.960	3.970	5.827	54.99	5.350	30.677
	MOEA/D	0.563	**0.791**	**0.601**	1.600	2.354	1.768	3.722	3.501	3.164	31.77	1.805	0.832

Note: 15°C, 25°C, 35°C indicate the ambient temperature, T_{amb}. All optimized parameters are obtained based on a weight factor w = [0.4 0.4 0.2] under Cycle #1.

in driving aggressiveness (i.e., from Cycle #1 to Cycle #3), the vehicle configuration derived from MOEA/D can better suppress the increase in energy consumption. Compared to an increase of energy consumption derived from NSGA2 (up to 101.7%) and SPEA2 (up to 224.7%), MOEA/D can limit the increase to 10.6%. It is worth mentioning that over the aggressive Cycle #3, the vehicle system improved by MOEA/D still can regulate cell temperature ISE well at different levels of the ambient temperature, while the other two algorithms are difficult to suppress.

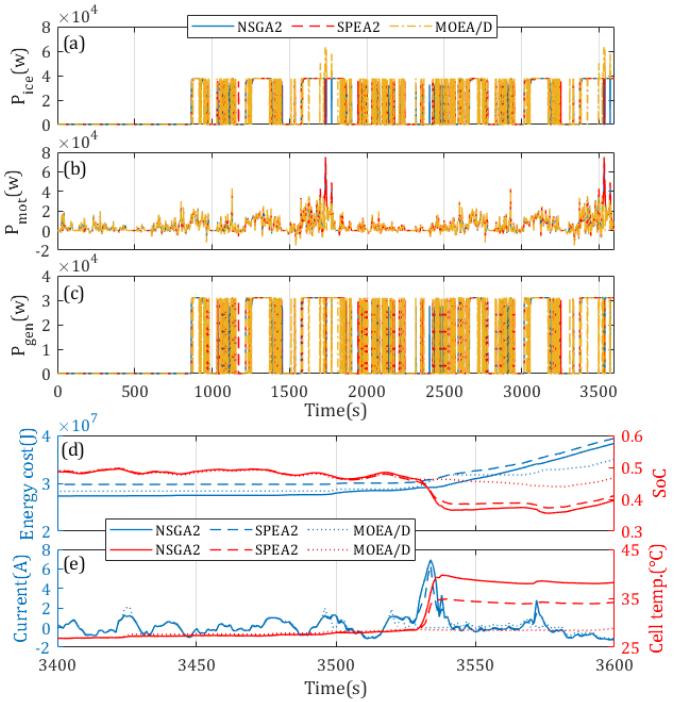

Fig. 7. Vehicle system performance over Cycle #3 with ambient temperature, T_{amb} = 25°C

To further explore the reasons behind this phenomenon, Fig. 7 presents representative time-dependent variables of the vehicle system over Cycle #3 with ambient temperature, T_{amb} = 25°C. Under the hybrid mode, the trends of energy flow of PHEV systems optimized by NSGA2, SPEA2, and MOEA/D are similar. When there is high power demand $t \in [1700,1800] \cup [3500,3600]$, the system with the proposed methodology will arrange for more power demand to be provided by the ICE, thereby reducing the peak power demand of the motor in this event. In this way, a transient surge of the cell temperature caused by the high-power demand of the motor can be avoided. Figs. 7(d)-(e) display the detailed real-time performance in one of peak power demand events $t \in [3400,3600]$. The overshooting of current of battery cells in the PHEV system optimized by SPEA2 is detected that would result in two potential problems. The first is continued battery high temperature may accelerate aging and reduce the efficiency of charge or discharge. The second is the low SoC may reduce the flexibility of energy-flow allocation to reduce the efficiency of the entire hybrid system. The PHEV system with MOEA/D ($T_{avg}^{\max}$ = 28.8°C, SoC_{end} = 0.46) can address these two problems much better than those with NSGA2 ($T_{avg}^{\max}$ = 34.8°C, SoC_{end} = 0.41) and SPEA2 ($T_{avg}^{\max}$ = 40.0°C, SoC_{end} = 0.40).

C. Modular Adaptation for Different Type Users

The mobility behavior within the population is extremely diverse. This section investigates the impact of different user types on the modular design and provides them with selection guidance. For the following analysis, three representative cases are selected as considered in [42]: user B has an annual mileage of 15,000 km, which is close to the German average. user C, as a frequent driver, travels double of this distance (30,000 km) and user A only half of this distance (7500 km), in which their speed trajectories are cropped in sequence by using repeated WLTCs (Cycle #1). Considering the daily commuting distance of the three user types, the studied vehicle system is modularly adapted to the desired component sizes and control parameters. In addition, the equivalent fuel consumption and maximum cell temperature of three user types are also explored under the different initial values of SoC.

TABLE IV
OPTIMIZED RESULT OF CONTROL PARAMETERS USED IN THE SYSTEM

User type	Power-split control parameters				
	$\phi_{1,\alpha}^*$	$\phi_{1,\beta}^*$	$\phi_{2,\alpha}^*$	$\phi_{2,\alpha}^*$	ϕ_{mode}^*
A	24.09	0.2688	0.1934	-1.195	5.822e+4
B	41.88	-2.794	8.201	-5.785	6.134e+4
C	11.61	0.5193	2.284	-5.456	4.712e+4

TABLE V
VEHICLE ADAPTABILITY PERFORMANCE OVER DIFFERENT TEST ENVIRONMENT

User type	Annual mileage (km)	Component size		EV range (km/d)	Hybrid range (km/d)
		ICE	Cells		
A	7500	2.0L	5000	13.34	7.30
B	15000	2.4L	4980	13.32	27.78
C	30000	1.8L	6034	23.55	58.64

Table IV & V organize optimized results of control and sizing parameters in modular adaptation with the PACO for three user types. For determining component sizes, on the premise of safe and efficient use of the PHEV system, we are trying to control the budget of the components (i.e., engine and battery pack) at a similar level, rather than blindly increase the size of energy resources. As an increase of annual mileage, the proportion of daily mileages in the hybrid mode grows gradually, ending at 71.3%. Compared with user type A, user type B utilizes a larger engine. The authors think the reason behind this is that the WLTC cycle used for user type A does not fully cover the ultra-high-speed section. User type B contains the entire complete speed sections, so increasing the size of the ICE allows doing more power compensation in the ultra-high-speed section. Since the daily mileage of user type C is twice that of user type B, a smaller ICE and more battery cells are employed for long mileage so that the rising rate of cell temperature during long-term driving can be reduced.

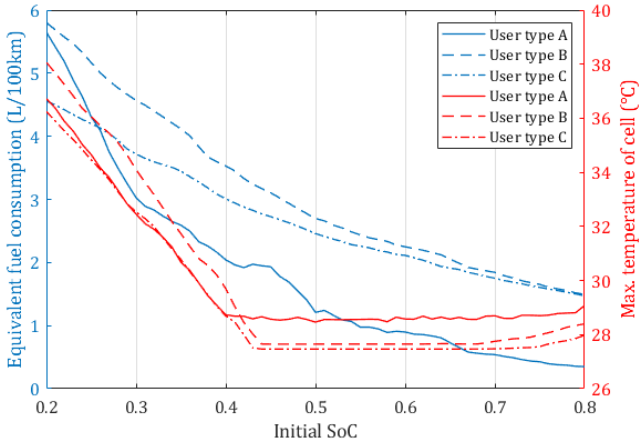

Fig. 8. Modular adaptation result of three different user types under the different initial values of SoC

Fig. 8 shows modular adaptation results including equivalent fuel consumption and maximum values of cell temperature under the different initial values of SoC, in which the sampling interval of the initial SoC is 0.1, $SoC \in [0.2,0.8]$. Generally, equivalent fuel consumption is decreasing as increasing the initial value of SoC. Specifically, the lowest equivalent fuel consumption is 0.4 L/100km for the user type A with the initial value of SoC at 0.8; the highest one is 5.8 L/100km for the user type B with the initial value of SoC at 0.2. In terms of maximum values of cell temperature, they linearly decrease to near the initial value of SoC at 0.4 at first and then stabilize until the initial value of SoC at 0.8. This is because before the inflection point occurs, the ICE needs to fast charge the battery to reach the safe and efficient operating range of SoC. Although the maximum value of cell temperature rises to a certain extent when the initial value of SoC is low, all the vehicle system optimized by the proposed methodology can regulate their cell temperatures ($27.5-38.3℃$) within a safe and efficient working zone ($0-55℃$). Considering the reliability of the optimized parameters, we are planning to conduct battery-in-the-loop experiments in the next stage for further evaluation.

VI. Conclusions

This paper proposes an improved modular design methodology with electrothermal dynamics conscious for a power-split PHEV. By introducing an advanced electrothermal battery model and a temperature-related sub-objective, this methodology simultaneously reveals battery thermal and electrical dynamics in the PHEV modular design. Validated by extensive numerical simulation with laboratory-made WLTCs, the performance of the proposed methodology is evaluated in terms of many-objective optimization, vehicle system robustness, and modular adaptation for different types of users. The conclusions drawn from the investigation are as follows:

1) For PHEV modular design, the PACO collects more non-dominated solutions, in which there is at least 28% of the increase compared to each single algorithm.
2) In the PACO, the MOEA/D is the main contributor because it lessens the generational distance by at least 2.7% and enlarges the hypervolume by at least 17.6%, compared to NSGA2 and SPEA2.
3) In the robustness testing of Cycle #2 and #3, the PHEV system using parameters optimized by MOEA/D controls an increase of the cost function value within 31.0%. That is much lower than increases of the cost function values using parameters optimized by NSGA2 (62.9%) and SPEA2 (77.1%).
4) In the modular adaptation for different user types, the PHEV system optimized by MOEA/D can regulate cell temperatures ($27.5-38.3℃$) of all user types within a safe and efficient working zone ($0-55℃$).

Appendix

The definitions of two used optimization metrics of the generational distance (GD) and hypervolume (HV) are presented, respectively. GD is used to evaluate the distance between estimated Pareto frontiers and their approximated Pareto frontier, which is calculated by [39]:

$$\mathrm{GD} = \frac{\sqrt{\sum_{m=1}^{N} y_m \cdot \mathrm{dis}^2(y_m, \boldsymbol{S}_{\mathrm{aPF}})}}{N} \qquad (A1)$$

where N is the member of elements in the ePF; y_m is the individual value in the ePF sets; $\boldsymbol{S}_{\mathrm{aPF}}$ is the Pareto front approximation; $\mathrm{dis}(y_m, \boldsymbol{S}_{\mathrm{aPF}})$ is the shortest distance between the element y_m and the approximated Pareto frontier.

The HV indicator is described as the volume of the space in the objective space dominated by the Pareto front approximation $\boldsymbol{S}_{\mathrm{aPF}}$ and delimited from above by a reference point $r \in R$ m such that for all $z \in \boldsymbol{S}_{\mathrm{aPF}}, z \prec r$. The HV indicator is given by [40]:

$$\mathrm{HV} = \Lambda_m \left(\bigcup_{z \in \boldsymbol{S}_{\mathrm{aPF}}} [z; r] \right) \qquad (A2)$$

where, Λ_m is the m-dimensional Lebesgue measure. The optimization problem has been stated in Section III for the three-objective case ($m = 3$).

References

[1] S. M. Shiva Nagendra, U. Schlink, V. Dheeraj Alshetty, M. Diya, and J. S. Menon, *Traffic-related air pollution, human exposure, and commercially available market solutions: Perspectives from the*

developing nation context, no. iii. Elsevier Inc., 2020.
[2] A. Mohamed, V. Salehi, T. Ma, G. S. Member, and O. A. Mohammed, "Real-Time Energy Management Algorithm for Plug-In Hybrid Electric Vehicle Charging Parks Involving Sustainable Energy," vol. 5, no. 2, pp. 577–586, 2014.
[3] J. Li *et al.*, "Pedestrian-Aware Supervisory Control System Interactive Optimization of Connected Hybrid Electric Vehicles via Fuzzy Adaptive Cost Map and Bees Algorithm," *IEEE Trans. Transp. Electrif.*, vol. 7782, no. c, pp. 1–1, 2021, doi: 10.1109/tte.2021.3124606.
[4] J. Oncken, K. Sachdeva, H. Wang, and B. Chen, "Integrated Predictive Powertrain Control for a Multimode Plug-in Hybrid Electric Vehicle," *IEEE/ASME Trans. Mechatronics*, vol. 26, no. 3, pp. 1248–1259, 2021.
[5] H. D. Potsch, "Volkswagen - Driving Forward," 2011.
[6] L. K. Gan, J. K. H. Shek, and M. A. Mueller, "Hybrid wind – photovoltaic – diesel – battery system sizing tool development using empirical approach , life-cycle cost and performance analysis : A case study in Scotland," *Energy Convers. Manag.*, vol. 106, pp. 479–494, 2015, doi: 10.1016/j.enconman.2015.09.029.
[7] D. H. Lee, N. W. Kim, J. R. Jeong, Y. I. Park, and S. W. Cha, "COMPONENT SIZING AND ENGINE OPTIMAL OPERATION LINE ANALYSIS FOR A PLUG-IN HYBRID ELECTRIC TRANSIT BUS," vol. 14, no. 3, pp. 459–469, 2013, doi: 10.1007/s12239.
[8] H. Kim and D. Kum, "Comprehensive Design Methodology of Input- and Output-Split Hybrid Electric Vehicles : In Search of Optimal Configuration," *IEEE/ASME Trans. Mechatronics*, vol. 21, no. 6, pp. 2912–2923, 2016.
[9] A. E. Bayrak, A. X. Collopy, B. I. Epureanu, and P. Y. Papalambros, "A Computational Concept Generation Method for a Modular Vehicle Fleet Design," 2016, doi: 10.1109/SYSCON.2016.7490619.
[10] Y. Huang *et al.*, "A review of power management strategies and component sizing methods for hybrid vehicles," *Renew. Sustain. Energy Rev.*, vol. 96, pp. 132–144, Nov. 2018, doi: 10.1016/J.RSER.2018.07.020.
[11] E. Silvas, T. Hofman, N. Murgovski, L. F. P. Etman, and M. Steinbuch, "Review of Optimization Strategies for System-Level Design in Hybrid Electric Vehicles," *IEEE Trans. Veh. Technol.*, vol. 66, no. 1, pp. 57–70, 2017, doi: 10.1109/TVT.2016.2547897.
[12] N. Murgovski, L. M. Johannesson, and J. Sjoberg, "Engine on/off control for dimensioning hybrid electric powertrains via convex optimization," *IEEE Trans. Veh. Technol.*, vol. 62, no. 7, pp. 2949–2962, 2013, doi: 10.1109/TVT.2013.2251920.
[13] A. Khalatbarisoltani, M. Kandidayeni, L. Boulon, and X. Hu, "Comparison of Decentralized ADMM Optimization Algorithms for Power Allocation in Modular Fuel Cell Vehicles," *IEEE/ASME Trans. Mechatronics*, pp. 1–12, 2021.
[14] J. Li, Q. Zhou, Y. He, H. Williams, H. Xu, and G. Lu, "Distributed Cooperative Energy Management System of Connected Hybrid Electric Vehicles with Personalized Non-Stationary Inference," *IEEE Trans. Transp. Electrif.*, vol. 7782, no. c, pp. 1–1, 2021, doi: 10.1109/tte.2021.3127142.
[15] J. Li, Q. Zhou, H. Williams, and H. Xu, "Back-to-back competitive learning mechanism for fuzzy logic based supervisory control system of hybrid electric vehicles," *IEEE Trans. Ind. Electron.*, vol. 67, no. 10, pp. 8900–8909, 2020, doi: 10.1109/TIE.2019.2946571.
[16] Q. Zhou *et al.*, "Modified Particle Swarm Optimization with Chaotic Attraction Strategy for Modular Design of Hybrid Powertrains," *IEEE Trans. Transp. Electrif.*, 2020, doi: 10.1109/TTE.2020.3014688.
[17] B. Chen, S. A. Evangelou, R. Lot, and A. Notation, "Series Hybrid Electric Vehicle Simultaneous Energy Management and Driving Speed Optimization," *IEEE/ASME Trans. Mechatronics*, vol. 24, no. 6, pp. 2756–2767, 2019.
[18] K. Liu, K. Li, Q. Peng, and C. Zhang, "A brief review on key technologies in the battery management system of electric vehicles," *Front. Mech. Eng.*, vol. 14, no. 1, pp. 47–64, 2019, doi: 10.1007/s11465-018-0516-8.
[19] Y. Wang *et al.*, "A comprehensive review of battery modeling and state estimation approaches for advanced battery management systems," *Renew. Sustain. Energy Rev.*, vol. 131, no. July, p. 110015, 2020, doi: 10.1016/j.rser.2020.110015.
[20] X. Hu, S. Li, and H. Peng, "A comparative study of equivalent circuit models for Li-ion batteries," *J. Power Sources*, vol. 198, no. November 2017, pp. 359–367, 2012, doi: 10.1016/j.jpowsour.2011.10.013.
[21] R. Xiong, J. Tian, W. Shen, and F. Sun, "A Novel Fractional Order Model for State of Charge Estimation in Lithium Ion Batteries," *IEEE Trans. Veh. Technol.*, vol. 68, no. 5, pp. 4130–4139, 2019, doi: 10.1109/TVT.2018.2880085.
[22] Y. Xie *et al.*, "An improved resistance-based thermal model for prismatic lithium-ion battery charging," *Appl. Therm. Eng.*, vol. 180, no. July, p. 115794, 2020, doi: 10.1016/j.applthermaleng.2020.115794.
[23] X. Hu, F. Feng, K. Liu, L. Zhang, J. Xie, and B. Liu, "State estimation for advanced battery management: Key challenges and future trends," *Renew. Sustain. Energy Rev.*, vol. 114, no. August, p. 109334, 2019, doi: 10.1016/j.rser.2019.109334.
[24] K. Liu, X. Hu, Z. Yang, Y. Xie, and S. Feng, "Lithium-ion battery charging management considering economic costs of electrical energy loss and battery degradation," *Energy Convers. Manag.*, vol. 195, no. February, pp. 167–179, 2019, doi: 10.1016/j.enconman.2019.04.065.
[25] J. Wu, Z. Wei, K. Liu, Z. Quan, and Y. Li, "Battery-Involved Energy Management for Hybrid Electric Bus Based on Expert-Assistance Deep Deterministic Policy Gradient Algorithm," *IEEE Trans. Veh. Technol.*, vol. 69, no. 11, pp. 12786–12796, 2020, doi: 10.1109/TVT.2020.3025627.
[26] K. Liu, C. Zou, K. Li, and T. Wik, "Charging pattern optimization for lithium-ion batteries with an electrothermal-aging model," *IEEE Trans. Ind. Informatics*, vol. 14, no. 12, pp. 5463–5474, 2018, doi: 10.1109/TII.2018.2866493.
[27] M. Ehsani, Y. Gao, S. Longo, and K. Ebrahimi, *Modern electric, hybrid electric, and fuel cell vehicles*. CRC press, 2018.
[28] A. Brooker *et al.*, "ADVISOR Advanced Vehicle Simulator," *National Renewable Energy Laboratory*, 2013. http://adv-vehicle-sim.sourceforge.net/.
[29] Guzzella, Lino and C. Onder, *Introduction to modeling and control of internal combustion engine systems*. Springer Science & Business Media, 2009.
[30] X. Lin *et al.*, "A lumped-parameter electro-thermal model for cylindrical batteries," *J. Power Sources*, vol. 257, no. July, pp. 12–20, 2014, doi: 10.1016/j.jpowsour.2014.01.097.
[31] C. Park and A. K. Jaura, "Dynamic Thermal Model of Li-Ion Battery for Predictive Behavior in Hybrid and Fuel Cell Vehicles," *SAE Tech. Pap.*, vol. 01, no. 2286, 2003, doi: 10.4271/2003-01-2286.
[32] Y. Xie, C. Wang, X. Hu, X. Lin, Y. Zhang, and W. Li, "An MPC-Based Control Strategy for Electric Vehicle Battery Cooling Considering Energy Saving and Battery Lifespan," *IEEE Trans. Veh. Technol.*, vol. 69, no. 12, pp. 14657–14673, 2020, doi: 10.1109/TVT.2020.3032989.
[33] C. Zou, X. Hu, Z. Wei, and X. Tang, "Electrothermal dynamics-conscious lithium-ion battery cell-level charging management via state-monitored predictive control," *Energy*, vol. 141, pp. 250–259, 2017, doi: 10.1016/j.energy.2017.09.048.
[34] J. Li, Q. Zhou, H. Williams, H. Xu, and C. Du, "Cyber-Physical Data Fusion in Surrogate-assisted Strength Pareto Evolutionary Algorithm for PHEV Energy Management Optimization," *IEEE Trans. Ind. Informatics*, 2021.
[35] M. Duvall, "Advanced Batteries for Electric-Drive Vehicles," 2004.
[36] S. Golbuff, "Optimization of a plug-in hybrid electric vehicle," Georgia Institute of Technology, 2006.
[37] G. Tian, Y. Ren, and M. Zhou, "Dual-Objective Scheduling of Rescue Vehicles to Distinguish Forest Fires via Differential Evolution and Particle Swarm Optimization Combined Algorithm," *IEEE Trans. Intell. Transp. Syst.*, vol. 17, no. 11, pp. 3009–3321, 2016, doi: 10.1109/TITS.2015.2505323.
[38] J. Zhou and X. Yao, "A hybrid approach combining modified artificial bee colony and cuckoo search algorithms for multi-objective cloud manufacturing service composition," *Int. J. Prod. Res.*, vol. 55, no. 16, pp. 4765–4784, 2017, doi: 10.1080/00207543.2017.1292064.
[39] K. Deb and J. Wiley, *Multi-objective optimization using evolutionary algorithms*. John Wiley & Sons, 2001.
[40] A. Auger, J. Bader, D. Brockhoff, and E. Zitzler, "Theory of the hypervolume indicator： Optimal μ-Distributions and the Choice of the Reference Point," in *Proceedings of the tenth ACM SIGEVO workshop on Foundations of genetic algorithms*, 2009, pp. 87–102, doi: 10.1145/1527125.1527138.
[41] J. Li, Q. Zhou, Y. He, H. Williams, and H. Xu, "Driver-identified

Supervisory Control System of Hybrid Electric Vehicles based on Spectrum-guided Fuzzy Feature Extraction," *IEEE Trans. Fuzzy Syst.*, vol. 6706, no. c, pp. 1–1, 2020, doi: 10.1109/tfuzz.2020.2972843.

[42] M. Redelbach, E. D. Özdemir, and H. E. Friedrich, "Optimizing battery sizes of plug-in hybrid and extended range electric vehicles for different user types," *Energy Policy*, vol. 73, pp. 158–168, 2014, doi: 10.1016/j.enpol.2014.05.052.

Ji Li (M'19) awarded the Ph.D. degree in mechanical engineering from the University of Birmingham, U.K, in 2020. He is currently a Research Fellow and works on the Connected and Autonomous Systems for Electrified Vehicles (CASE-V) at the Birmingham CASE-V Automotive Research and Education Centre. His current research interests include computational intelligence, bioinformatic fusion, data-efficient modelling, feature selection, man-machine system, and their applications on connected and autonomous vehicles.

Kailong Liu (M'19) earned his Ph.D. degree in electrical engineering from the Energy, Power, and Intelligent Control group, Queen's University Belfast, U.K, in 2018. He is currently an assistant professor in the Warwick Manufacturing Group, University of Warwick, U.K. His research interests include modeling, optimization, and control, with applications to electrical/hybrid vehicles, energy storage, and battery management systems. Dr. Liu is on editorial boards of some journals of his area including Renewable and Sustainable Energy Reviews, IEEE/CAA Journal of Automatica Sinica, Control Engineering Practice.

Quan Zhou (M'17) received the Ph.D. degree in mechanical engineering from the University of Birmingham in 2019 that was distinguished by being the sole recipient of the University's Ratcliffe Prize of the year. He is currently an assistant professor in automotive engineering and leads the research into Connected and Autonomous Systems for Electrified Vehicles at the University of Birmingham. His research interests include evolutionary computation, fuzzy logic, reinforcement learning, and their applications in vehicular systems.

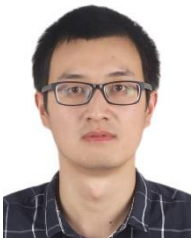

Jinhao Meng (M'19) received the Ph.D. degree in electrical engineering from Northwestern Polytechnical University, Xi'an, China, in 2019. He was supported by the China Scholarship Council as a joint Ph.D. student with the Department of Energy Technology, Aalborg University, Aalborg, Denmark. He is currently an associate researcher in Sichuan University, Chengdu, China. His research interests include battery modeling, battery states estimation, and energy management of battery energy storage system.

Yunshan Ge is a full Professor of Mechanical Engineering at the Beijing Institute of Technology, Beijing, China. He received the Ph.D. degree in Thermal Physics from the Jilin University of Technology. Since graduating in 1994, he has long been engaged in researching policies and regulations related to the formation mechanisms of motor vehicle pollutants and control technologies, participated in revising China main mobile source emission standards, and published more than 300 academic papers.

Hongming Xu received the Ph.D. degree in mechanical engineering from Imperial College London, London, U.K. He is a full Professor of Energy and Automotive Engineering at the University of Birmingham, Birmingham, U.K., and Head of Vehicle and Engine Technology Research Centre. He has six years of industrial experience with Jaguar Land Rover. He has authored and co-authored more than 500 journal and conference publications on advanced vehicle powertrain systems involving both experimental and modeling studies.